

# Co-formation of the thin and thick discs revealed by APOGEE-DR16 and *Gaia*-DR2

Leandro Beraldo e Silva<sup>1\*</sup>, Victor P. Debattista<sup>1</sup>, David Nidever<sup>2,3</sup>,  
João A. S. Amarante,<sup>4</sup> and Bethany Garver<sup>2</sup>

<sup>1</sup>*Jeremiah Horrocks Institute, University of Central Lancashire, Preston, PR1 2HE, UK*

<sup>2</sup>*Department of Physics, Montana State University, P.O. Box 173840, Bozeman, MT 59717-3840*

<sup>3</sup>*NSF's National Optical-Infrared Astronomy Research Laboratory, 950 North Cherry Ave, Tucson, AZ 85719*

<sup>4</sup>*Key Laboratory for Research in Galaxies and Cosmology, Shanghai Astronomical Observatory, Chinese Academy of Sciences, 80 Nandan Road, Shanghai 200030, China*

Accepted XXX. Received YYY; in original form ZZZ

## ABSTRACT

Since thin disc stars are younger than thick disc stars on average, some Galaxy formation models predict that the thin disc started forming only after the thick disc had formed, around 10 Gyr ago. Accordingly, no significant old thin disc population should exist. Using 6-D coordinates from *Gaia*-DR2 and age estimates from Sanders & Das (2018), we select  $\sim 24000$  old stars ( $\tau > 10$  Gyr, with uncertainties  $\lesssim 15\%$ ) within 2 kpc from the Sun. A cross-match with APOGEE-DR16 reveals comparable fractions of old thin/thick disc stars. We show that the sample pericenter radius ( $r_{\text{per}}$ ) distribution has three peaks, one associated with the stellar halo and the other two having contributions from the thin/thick discs. Using a high-resolution  $N$ -body+Smooth Particle Hydrodynamics simulation, we demonstrate that one peak, at  $r_{\text{per}} \approx 7.1$  kpc, is produced by stars from both discs which were born in the inner Galaxy and migrated to the Solar Neighbourhood. We estimate that, in the Solar Neighbourhood,  $\sim 1/2$  ( $\sim 1/3$ ) of the old thin (thick) disc stars can be classified as migrators. Our results suggest that thin/thick discs are affected differently by radial migration inasmuch as they have different eccentricity distributions, regardless of vertical scale heights. Finally, we interpret the existence of a significant old thin disc population as evidence for an early co-formation of thin/thick discs, arguing that clump instabilities in the early disc offer a compelling explanation for the observed trends.

**Key words:** Galaxy: formation – Galaxy: evolution – Galaxy: structure – Galaxy: disk – Galaxy: abundances – galaxies: abundances

## 1 INTRODUCTION

The Milky Way (MW) disc is a compound structure, as first revealed by its double exponential vertical density profile (Yoshii 1982; Gilmore & Reid 1983). The thin disc is characterized by stars on low-eccentricity orbits and which, on average, are younger than the thick disc. In turn, the thick disc is more centrally concentrated, has a larger fraction of stars on eccentric orbits and is older on average (see e.g. Bovy et al. 2012; Mackereth et al. 2019; Ciucă et al. 2020). Additionally, the MW chemical abundance map ( $[\alpha/\text{Fe}]$  vs  $[\text{Fe}/\text{H}]$ ) is bi-modal, with  $\alpha$ -rich stars being more vertically extended, in contrast to  $\alpha$ -poor stars, and thus associated

with the geometrical thick disc<sup>1</sup> (e.g. Adibekyan et al. 2011; Bensby et al. 2014; Anders et al. 2014; Nidever et al. 2014).

Because the thick disc is old, modelling its formation is intrinsically related to dating the earliest events in the Galaxy's evolution, and several possibilities have been considered, including the early accretion from disrupted satellites (Abadi et al. 2003), heating of a proto-disc by a major merger (Quinn et al. 1993; Kazantzidis et al. 2008; Villalobos & Helmi 2008; Helmi et al. 2018), in-situ star formation following a gas-rich merger (Brook et al. 2004), scattering by clumps in an early gas-rich phase (Bournaud et al. 2009;

<sup>1</sup> However, note that the discs defined chemically and geometrically are not related one-to-one. In this work we adopt the chemical definition.

\* E-mail: lberaldosilva@uclan.ac.uk (LBS)

Clarke et al. 2019; Beraldo e Silva et al. 2020), radial migration (Schönrich & Binney 2009b; Loebman et al. 2011), direct in-situ formation from a turbulent thick gas disc (so called “upside-down” formation – Bird et al. 2013), mergers with subsequent cosmological inflow of gas along filaments (Agertz et al. 2020) and the rapidly changing orientation of the galactic plane (Meng & Gnedin 2020).

While some of these scenarios (notably the upside-down) predict a sequential formation, with the geometric thin disc significantly forming only after the thick disc, in other scenarios the thin disc is expected to start forming simultaneously with the thick disc, with the consequence that a significant population of old thin disc stars should exist. For instance, Abadi et al. (2003) predict that  $\approx 15\%$  of currently (kinematically defined) thin disc stars should have ages  $\tau > 10$  Gyr in the accretion scenario, while in the major merger picture, the geometric thin remnant of the heated disc should represent  $15\% - 25\%$  of the total stellar mass at the end of the merger, according to Villalobos & Helmi (2008). Additionally, in the clumpy formation scenario, the early disc develops clumps, which heat stars vertically (as originally shown by Bournaud et al. 2009) and enrich the medium with  $\alpha$ -elements, producing a chemical bi-modality (as shown by Clarke et al. 2019) and geometric thin+thick discs similar to those observed in the MW (as shown by Beraldo e Silva et al. 2020). Thus, thin+thick disc co-formation and an old thin disc population are natural predictions of this scenario.

Whatever may be the case for the thin disc’s early formation, there is evidence for it growing inside-out (as in, e.g., Chiappini et al. 2001; Muñoz-Mateos et al. 2007; Bovy et al. 2016) at later times, i.e. stars forming at progressively larger radii, with the consequence that, at a fixed time, due to their faster metal-enrichment, stars born at smaller radii are typically more metal-rich than those formed in the outer part of the disc. The observation of these trends is complicated by radial migration (churning), which can move stars inwards or outwards by several kpc on short timescales. This mechanism changes the angular momenta of individual stars without changing their radial actions and is more efficient for nearly-circular orbits (see Sellwood & Binney 2002; Roškar et al. 2012). An important consequence is a net movement outward of more metal-rich inner stars, as detected, e.g., in APOGEE (Hayden et al. 2015), LAMOST+RAVE+Gaia-DR1 (Vickers & Smith 2018) and in simulations (Loebman et al. 2016) – see also Schönrich & Binney (2009a).

Recently, Prudil et al. (2020) found evidence for a population of 22 RR Lyrae stars (which are older than 10 Gyr – see e.g. Glatt et al. 2008; VandenBerg et al. 2013) with pericenter radii peaking at  $r_{\text{per}} \approx 7$  kpc, small vertical excursions ( $z_{\text{max}} < 0.9$  kpc), high metallicities and low  $\alpha$ -abundances, which they deemed a ‘conundrum’: how can an old population have chemical and kinematic properties typical of the thin disc? And how, in apparent contradiction with an inside-out growth, would this old population be located at such large radii?

In this work, using the catalogue of Sanders & Das (2018), in conjunction with chemical abundances from APOGEE-DR16 (Ahumada et al. 2020; Jönsson et al. 2020), we confirm the existence of a significant population of old ( $\tau > 10$  Gyr) thin disc stars in the Solar Neighbourhood and the presence of a peak in the pericenter radii at  $r_{\text{per}} \approx 7$  kpc

with contributions from both thin and thick discs. We further interpret the existence of an old thin disc population as evidence for an early co-formation of the thin and thick discs, with the  $r_{\text{per}}$  peak produced by radial migration of both components. In Sec. 2, we present our data sample and explain the orbit integration procedure, as well as the assumed Galaxy model. In Sec. 3 we present our results supporting an early co-formation of the thin and thick discs. The location of the  $r_{\text{per}}$  peak is investigated by means of a  $N$ -body+SPH simulation in Sec. 4, where we show that these stars must have formed in the inner disc and end up at larger radii due to radial migration. In Sec. 5 we discuss the implications of this finding for different scenarios of the early evolution of the MW and, in particular, for the thick disc. We also discuss the differences of radial migration in the thin and thick discs and how our results solve the apparent conundrum of thin disc RR Lyrae stars. Finally, we summarize our conclusions in Sec. 6.

## 2 OBSERVATIONAL DATA AND ORBIT INTEGRATION

We explore the extraordinary astrometric data from *Gaia*-DR2 and age estimates from the value-added catalogue of Sanders & Das (2018). This catalogue is based on data from several spectroscopic surveys and provides distance, mass and age estimates for  $\sim 3$  million stars. The catalogue also provides Galactocentric cylindrical coordinates and velocities and, when available, IDs of stars identified in the spectroscopic surveys. We refer the reader to the original paper for details.

From this catalogue, we select stars in the subsamples of giants (defined as  $\log g > 3$  dex and  $\log_{10}(T_{\text{eff}}/K) < 3.73$ ), and turnoff stars (defined as  $3.6 < \log g < 4.5$  and  $\log_{10}(T_{\text{eff}}/K) < 4.1$ ), for which the ages are most reliable, according to Sanders & Das (2018). We select old stars ( $\tau > 10$  Gyr) within a distance from the Sun  $d < 2$  kpc and require age uncertainties  $\sigma_{\tau} < 1.5$  Gyr. Additionally, we require accurate parallaxes ( $|\varpi/\sigma_{\varpi}| > 5$ ) and line-of-sight velocities ( $|v_{\text{los}}/\sigma_{v_{\text{los}}}| > 5$ ). Note that this last requirement suppresses stars with small  $v_{\text{los}}$ , even if  $\sigma_{v_{\text{los}}}$  is as small as 1 km/s, mainly suppressing the contribution of near-by thin disc stars. Thus, this is a conservative cut for the detection of a significant population of old thin disc stars and does not affect the conclusions of our work. In order to avoid stars with age uncertainties which are too small, and which are artificially produced by the model isochrone gridding, we require  $\sigma_{\log_{10} \tau} > 0.015$  dex, as suggested by Sanders & Das (2018). Finally, we restrict to stars with the flag `best=1` (stars with a match in *Gaia* and no duplicate observations or observational problem detected). This results in a sample of 23,857 stars, with a median age uncertainty of 0.99 Gyr (and maximum uncertainty of 1.5 Gyr, defined in the quality cut).

We use the phase-space coordinates of our sample as initial conditions and, using the AGAMA package (Vasiliev 2019), integrate the orbits in the Galactic potential model of McMillan (2017). We identify 62 unbounded stars, which we exclude, leaving a sample with 23,795 bound stars. Each orbit is integrated forwards for 10 dynamical times (i.e. for  $\sim 2$  Gyr), and we calculate the pericenter and apocenter radii,

$r_{\text{per}}$  and  $r_{\text{apo}}$ , respectively. The eccentricity is estimated as

$$e = \frac{r_{\text{apo}} - r_{\text{per}}}{r_{\text{apo}} + r_{\text{per}}}. \quad (1)$$

Finally, for each orbit we also calculate the maximum height from the Galactic plane  $z_{\text{max}}$ .

Additionally, when further splitting the data into thick and thin discs, we cross-match with APOGEE-DR16 (Ahumada et al. 2020; Jönsson et al. 2020), resulting in a sample of  $\sim 1000$  stars with accurate metallicities and  $\alpha$ -abundances. Rojas-Arriagada et al. (2019) showed that magnesium is the  $\alpha$ -element with most reliable abundance estimates in APOGEE and we therefore use  $[\text{Mg}/\text{Fe}]$  to trace the  $\alpha$ -abundances.

### 3 OBSERVATIONAL RESULTS

We now show the results obtained from our sample of old stars in the Solar Neighbourhood. We start analyzing the distribution of eccentricities and pericenter radii, demonstrating the presence of three peaks, one of which is at  $r_{\text{per}} \approx 7$  kpc. In Sec. 3.2, we cross-match the data with the APOGEE-DR16, split the resulting sample into chemical thin and thick discs and investigate the chemo-kinematic properties of these components, showing their relative contributions to the  $r_{\text{per}}$  peaks. In Sec. 3.3 we present the first evidence that the peak at  $r_{\text{per}} \approx 7$  kpc is produced by radial migration. This is further investigated with a high-resolution simulation in Sec. 4.

#### 3.1 Peaks in pericenter radius

Fig. 1, upper panel, shows contours for eccentricity versus pericenter radius for our sample. The dashed lines represent two fixed values of apocenter radius  $r_{\text{apo}}$  – see Eq. 1. The absence of data with  $r_{\text{apo}} < 6$  kpc reflects the selection of stars within  $d < 2$  kpc from the Sun, given the Solar position  $R_{\odot} \approx 8$  kpc, while the vast majority of the stars have  $r_{\text{apo}} < 14$  kpc. The distribution peaks along a line of approximately constant  $r_{\text{apo}}$ , in  $8 \lesssim r_{\text{apo}}/\text{kpc} \lesssim 9$ , which also must be a selection effect given the Solar position and the larger time stars spend near their apocenters. The contours suggest the presence of three peaks: the first at  $(r_{\text{per}}, e) \approx (0.5 \text{ kpc}, 0.9)$ , the second at  $\approx (5-6 \text{ kpc}, 0.25)$  and the third at  $\approx (7 \text{ kpc}, 0.1)$ .

The lower panel shows the kernel density estimate (KDE) of  $r_{\text{per}}$  (i.e. of the projection of the upper panel on the  $x$ -axis) using a Gaussian kernel with window width  $h = 0.07$ , which was chosen by cross-validation (solid grey), where the three peaks mentioned before can be seen more clearly. In order to eliminate stars with extreme or unrealistic kinematic properties, which can arise because of the assumed model for the MW's potential, we select stars with  $6 < r_{\text{apo}}/\text{kpc} < 14$ , i.e. between the dashed curves in the upper panel. The  $r_{\text{per}}$  KDE for stars that satisfy this cut (black dashed in the lower panel) is very similar to that of the total sample, with the only noticeable difference being a small suppression of high eccentricity orbits in the first peak. Since this peak is not relevant for the analysis here, as explained below, in the rest of the paper we use this restricted sample ( $N = 22,776$  stars).

In order to check for the real significance of the peaks,

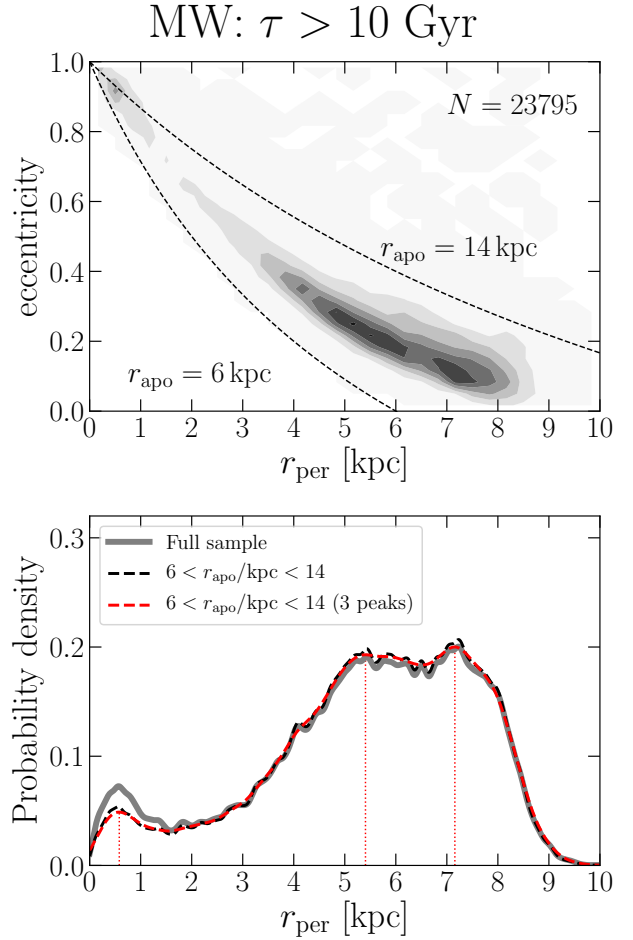


**Figure 1.** Top: distribution of old (turnoff + giant) stars in eccentricity,  $e$ , vs pericentric radius,  $r_{\text{per}}$ , calculated with age estimates and astrometric data from Sanders & Das (2018) – see Sec. 2. Bottom: KDEs of  $r_{\text{per}}$ : for the full sample (grey), for  $6 < r_{\text{apo}}/\text{kpc} < 14$  (black dashed) and for this region and the most detailed KDE producing 3 peaks (dashed red) at the positions shown by vertical lines (see the text for details). A statistical test rules out models with less than 3 peaks.

as opposed to random fluctuations, we perform the test proposed by Silverman (1981). This test is based on the number of peaks produced by KDEs of the data with varying window widths. A very small window width produces a KDE with many peaks, possibly over-fitting the data, while a KDE with a large window width produces a reduced number of peaks, possibly erasing important structure in the data. The null hypothesis  $H_0$  to be tested is that the distribution has  $k$  peaks against the hypothesis  $H_1$  that it has  $k + 1$  or more peaks. The test algorithm is as follows: for each number  $k$  of peaks to be tested, starting from one, we define the critical window width  $h_{\text{crit}}$  as the minimum width to produce at most  $k$  peaks. Then we check the statistical significance of this  $h_{\text{crit}}$  by bootstrap, re-sampling the data and calculating a new  $h_{\text{crit}}^*$  for each sample. At a given statistical significance  $\alpha$ , we reject  $H_0$  if, for an appropriate quantity  $\lambda_\alpha$ , the probability  $P(h_{\text{crit}}^*/h_{\text{crit}} > \lambda_\alpha) > 1 - \alpha$ . The main advantage of this method is that it is very generic, thus avoiding the assump-

$k$	$h_{\text{crit}}$	$P_{\text{Silverman}}$	$P_{\text{HY}}$
1	0.632	$\approx 1.$	$\approx 1.$
2	0.530	$\approx 1.$	$\approx 1.$
3	0.207	0.523	0.662

**Table 1.** Results for the test of statistical significance of  $r_{\text{per}}$  peaks in Fig. 1. The first column ( $k$ ) is the number of peaks to be tested; the second column indicates the critical bandwidth, i.e. the minimum to produce at most  $k$  peaks; the third column shows the probability for the number of peaks to be larger than  $k$  in the original test of Silverman (1981); the forth column shows the probabilities after the correction/calibration of Hall & York (2001). Models with  $P > 0.95$  can be excluded.

tion of Gaussianity, inherent in Bayesian Information Criterion (BIC) and Akaike Information Criterion (AIC) tests under a Gaussian Mixture Model – see Ivezić et al. (2014). Note that by “peak” we mean a local maximum, as opposed to a “bump” which is an interval where the curve is concave (seen from below) but not necessarily a local maximum.

In the original test proposed by Silverman (1981),  $\lambda_\alpha = 1$ , and this test is known to be conservative, i.e. less restrictive in rejecting models. For 1000 bootstrap samples, we obtain the probabilities shown in the third column of Table 1. Despite the conservativeness of the test, models with  $k = 1$  or  $k = 2$  peaks can still be rejected with high significance. Correcting and calibrating this test, Hall & York (2001) obtained  $\lambda_\alpha \approx 1.13$  for  $\alpha = 0.05$ . Although this calibration applies strictly to test for uni-modality ( $k = 1$ ), we also use it to test for larger numbers of peaks, obtaining the probabilities shown in the forth column of Table 1. Once more, models with  $k = 1$  or  $k = 2$  peaks can be rejected with high significance, while a model with  $k = 3$  peaks cannot be excluded. Thus, the presence of (at least) three peaks is confirmed with high statistical significance. This confirms the findings of Prudil et al. (2020), who also detected the presence of three peaks, although under the assumption of Gaussian components and with a restricted sample (314 RR Lyrae stars). This shows that this  $r_{\text{per}}$  distribution is not associated with any specific feature of their sample, but indicates the presence of distinct Galactic components.

The red dashed curve in Fig. 1 (lower panel) is the  $r_{\text{per}}$  KDE obtained with the  $h_{\text{crit}}$  for three peaks from Table 1, i.e. it represents the most detailed KDE having no more than three peaks. The only, barely noticeable, difference with respect to the black curve is the smoothing of the little wiggles. The three peaks are located at  $r_{\text{per}} \approx 0.59$  kpc, 5.4 kpc and 7.14 kpc (as indicated by the vertical red dotted lines).

Next, we analyze the chemical and kinematic properties of stars in these three populations and use the results to suggest their association with known structures in the MW.

### 3.2 Halo, thick and thin discs

The catalogue of Sanders & Das (2018) provides ages, 6-D phase space coordinates and metallicities, but lacks information on the  $\alpha$ -abundances. For this, we cross-match the sample with APOGEE-DR16, which results in 1049 (turnoff + giant) stars. The chemical abundances ( $[\text{Mg}/\text{Fe}]$  and  $[\text{Fe}/\text{H}]$ ) for these stars from APOGEE-DR16 are shown in Fig. 2 (upper panel). Colours represent the different populations represented by the separating straight lines (defined by eye,

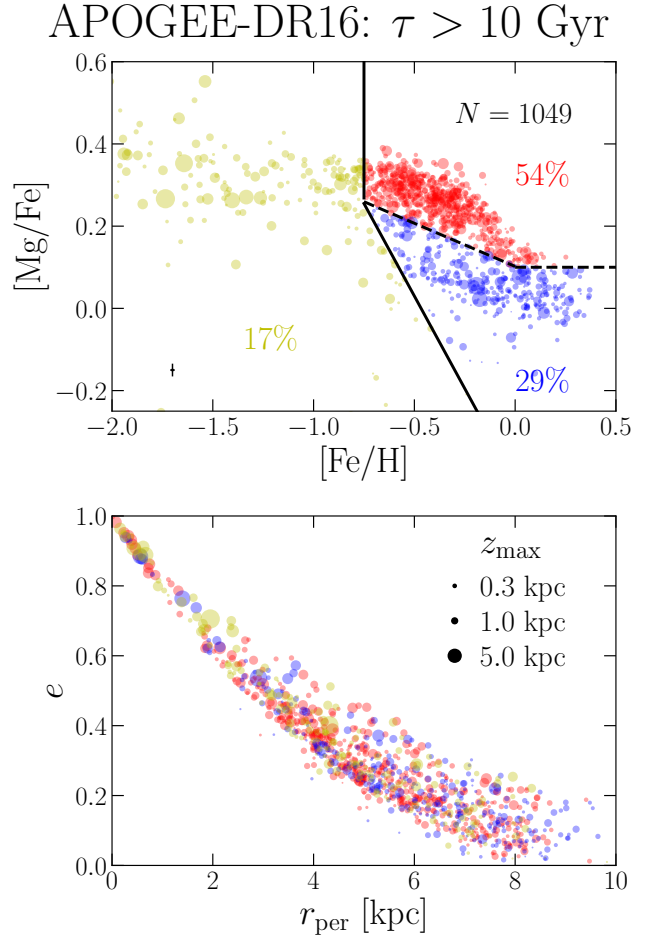


**Figure 2.** Chemical map (top) and eccentricity,  $e$ , vs pericenter radius,  $r_{\text{per}}$ , distribution (bottom), for the cross-match with APOGEE-DR16. Colours represent different populations, split using the straight lines, defining the halo (yellow), thick (red) and thin (blue) discs, with the fractions of each component shown in the top panel. Point sizes are proportional to  $z_{\text{max}}$ . The black point in the top panel shows the median uncertainties in  $[\text{Fe}/\text{H}]$  and  $[\text{Mg}/\text{Fe}]$ . Considering the peaks in Fig. 1, the first (from left to right) is predominantly associated to the halo ( $\alpha$ -rich, very metal-poor and high  $z_{\text{max}}$ ), while the second and third have significant contributions from the thick disc ( $\alpha$ -rich, reasonably metal poor and intermediate  $z_{\text{max}}$ ) and the thin disc ( $\alpha$ -poor, metal-rich and small  $z_{\text{max}}$ ). The top panel suggests that the thin/thick discs were co-forming in the MW’s very first Gyrs, with comparable star counts.

similarly to the definitions of e.g. Adibekyan et al. 2011; Mackereth et al. 2019), which define regions for the stellar halo (yellow), thick disc (red) and thin disc (blue). The black point at the bottom left illustrates the median uncertainties in  $[\text{Mg}/\text{Fe}]$  and  $[\text{Fe}/\text{H}]$ , as reported in APOGEE-DR16. The lower panel shows the distribution of these stars in the  $e$  vs  $r_{\text{per}}$  plot. In the two panels, point sizes are proportional to  $z_{\text{max}}$ .

The most metal-poor and generally  $\alpha$ -rich stars (yellow points) occupy the locus, in the chemical map, identified with the halo. These stars are typically clustered around small  $r_{\text{per}}$  and high  $e$ , and have large vertical excursions, with

$z_{\max}$  reaching  $\gtrsim 10$  kpc, which is consistent with our assignment of these stars to the stellar halo, with a probable accreted origin, as argued by Belokurov et al. (2018) and Helmi et al. (2018). The red points represent stars with chemical abundances typical of the thick disc, i.e. they are  $\alpha$ -rich and reasonably metal-poor. These stars spread across all values of  $e$  and  $r_{\text{per}}$  in the lower panel, but seem to cluster around  $r_{\text{per}} \approx 5$  kpc and  $e \approx 0.25$ . Additionally, these stars have  $z_{\max}$  as large as a few kpc, which is also consistent with their classification as thick disc stars. Finally, the  $\alpha$ -poor, metal-rich stars (blue points) spread around  $4 \lesssim r_{\text{per}}/\text{kpc} \lesssim 8$  and  $e \approx 0.2$  and typically have small vertical excursions  $z_{\max}$ , compatible with their assignment to the thin disc.

At first sight the features just listed would suggest the identification, from left to right in Fig. 1, of the first  $r_{\text{per}}$  peak with halo stars, the second peak with the thick disc and the third peak with the thin disc. However, a closer inspection shows that both the thin and thick disc components contribute distinctively to each of the second and third  $r_{\text{per}}$  peaks, as we show in Sec. 3.3. Whatever the case may be, the identification of three peaks, seemingly associated to the halo, thin and thick discs, agrees with the results from Prudil et al. (2020), although the position of the second peak differs from the value  $r_{\text{per}} \approx 3$  kpc found in that work. This reinforces their conclusion about the detection of the third peak and its main relation to an old thin disc population, while showing that it is not associated to any specific feature of their sample, but it represents a significant Galactic component.

Our separation in the chemical space shown in Fig. 2 results in  $\sim 17\%$  of the stars in the halo,  $\sim 54\%$  in the thick disc and  $\sim 29\%$  in the thin disc. However, these fractions should not be considered as precisely describing the whole Galaxy, since precise fractions would require a detailed analysis of the APOGEE-DR16 selection function, which is beyond the scope of this work. In the Appendix we apply different simple geometric and age cuts and show that the fractions of old thin and thick disc stars typically vary around  $\sim 20 - 30\%$  and  $\sim 40 - 55\%$ , respectively – see Table A1.

Most importantly, since  $[\text{Fe}/\text{H}]$  and  $[\text{Mg}/\text{Fe}]$  are conserved over a star's life-time, Fig. 2 shows that already in the very first Gyrs of the MW's evolution, not only the thick disc but *both* chemical thin and thick discs were forming, with comparable star counts. The conclusion is similar, although with a poorer statistics, if we select stars older than 11 Gyr. In this case, the cross-match with APOGEE-DR16 results in only 573 stars (with median age uncertainty of  $\approx 0.84$  Gyr). Of these, 21% belong to the halo, 54% to the thick disc and 25% to the thin disc – see Table A1. In Sec. 5, we develop this conclusion and discuss the implications for various scenarios of the formation of the thick disc.

In what follows, we focus on the thin and thick discs. When referring to the  $r_{\text{per}}$  peaks (see lower panel of Fig. 1), we neglect the left-hand peak associated to the stellar halo, and call the two remaining peaks, at  $r_{\text{per}} \approx 5.4$  kpc and  $r_{\text{per}} \approx 7.14$  kpc, the low and high  $r_{\text{per}}$  peaks, respectively.

### 3.3 Migrators and non-migrators in the thin and thick discs

Fig. 3 shows the KDEs of chemical and kinematic quantities for the thick disc (upper panel) and thin disc (lower panel).

First, in the left-hand column, we note that the thin disc  $r_{\text{per}}$  distribution has two peaks, one at  $r_{\text{per}} \approx 5$  kpc and another at  $r_{\text{per}} \approx 7$  kpc, while the thick disc peaks at  $r_{\text{per}} \approx 5$  kpc and has a bump at  $r_{\text{per}} \approx 7$  kpc. This shows that the low and high  $r_{\text{per}}$  peaks (second and third, from left to right in Fig. 1) have distinct contributions from both the thin and thick discs, although the thick disc contributes mostly to the low  $r_{\text{per}}$  peak, while the thin disc gives similar contributions to the low and high  $r_{\text{per}}$  peaks. This contrasts with the conclusions of Prudil et al. (2020), who tentatively attribute the low  $r_{\text{per}}$  peak to the thick disc and the high  $r_{\text{per}}$  peak to the thin disc.

Using a Gaussian Mixture Model (GMM) (Pedregosa et al. 2011), we split the thin and thick discs  $r_{\text{per}}$  distributions into three Gaussians each, although only showing the two relevant components (the third Gaussian, not shown, lies at small  $r_{\text{per}}$  and large  $e$  and is probably due to contamination from the halo). These Gaussian components are shown as dashed and dotted lines in the first column of Fig. 3. With these Gaussians, we define two subsamples, according to the highest probability of belonging to one or the other Gaussian component. In the other columns, the dashed and dotted lines represent the KDEs of the corresponding quantities for these fixed subsamples.

The second column shows that the thin disc eccentricity distribution peaks at  $e \approx 0.2$  and extends to  $e \lesssim 0.7$ , while the thick disc eccentricity distribution peaks at  $e \approx 0.25$  and is slightly broader. For both discs, the high (low)  $r_{\text{per}}$  subsample is characterized by lower (higher) eccentricities. In principle, this could be seen as a simple manifestation of the anti-correlation between  $r_{\text{per}}$  and eccentricity expressed by Eq. (1) and shown in Figs. 1 and 2. However, the presence of the  $r_{\text{per}}$  peaks and bumps (in both discs) indicates the existence of a distinct population with  $r_{\text{per}} \approx 7.1$  kpc, and these results show that this population is characterized by nearly-circular orbits.

The KDEs for  $[\text{Fe}/\text{H}]$  and  $[\text{Mg}/\text{Fe}]$  (third and fourth columns) show that, for both the thin and thick discs, the two Gaussian  $r_{\text{per}}$  components (dashed and dotted curves) have chemical distributions similar to that of the total sample (thick solid), thus indicating that the  $r_{\text{per}}$  subsamples are typical thin or thick disc samples, and not due to cross contamination.

Although the origin of the high  $r_{\text{per}}$  peak will be investigated further in Sec. 4.3 (where the same  $r_{\text{per}}$  distributions are reproduced in a simulation), the results just presented allow us to anticipate that this peak is due to radial migration of stars near corotation of spiral patterns (churning). In fact, nearly-circular orbits are the ones for which radial migration is most effective (Sellwood & Binney 2002; Roškar et al. 2012). Additionally, radial migration does not heat the orbits, i.e. it does not increase their eccentricities. This further suggests that stars contributing to the high  $r_{\text{per}}$  peak migrated to their current location while preserving low eccentricities. Therefore, we call the stars composing the high  $r_{\text{per}}$  peak the *migrators*, and the ones composing the low  $r_{\text{per}}$  peak the *non-migrators* – see Sec. 4.3. In the GMM, 55% of the thin disc stars are classified as migrators, while this fraction decreases to 38% for thick disc stars – see Fig. 3.

Finally, the right-hand column shows that the thin and thick discs have similar  $z_{\max}$  distributions, peaking at  $0.5 \lesssim z_{\max}/\text{kpc} \lesssim 1$ . Importantly, there is a large fraction of chemical thick disc stars occupying the region associated to

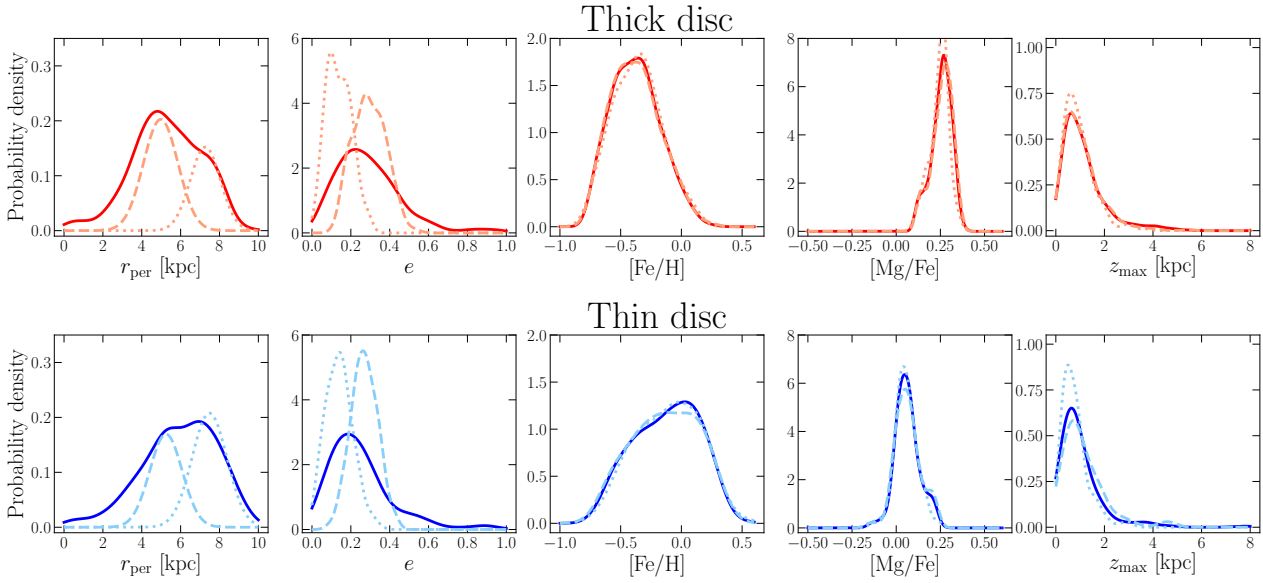


**Figure 3.** KDEs for kinematic quantities and chemical abundances for the thin and thick discs in the MW from APOGEE-DR16. The  $r_{\text{per}}$  distribution has two peaks/bumps for both discs, which we model as two Gaussian components, shown in the first column as dotted and dashed curves. In the other columns, dotted and dashed curves show the KDEs of the respective quantities for these two subsamples. The larger  $r_{\text{per}}$  subsample (dotted) is characterized by lower eccentricities while the lower  $r_{\text{per}}$  subsample (dashed lines) is characterized by higher eccentricities. The chemical abundance distributions of these subsamples are very similar to that of the total sample inside each disc, suggesting that the  $r_{\text{per}}$  peaks/bumps are not due to contamination from the thin/thick discs.

the geometric thin disc, i.e. at small  $z_{\text{max}}$ . This large fraction is partially due to the adopted geometric cut ( $d < 2$  kpc), which naturally suppresses the high  $z_{\text{max}}$  portion of the thick disc. However, in the Appendix we show that even selecting stars with  $|z| < 6$  kpc, the fraction of chemical thick disc stars with low  $z_{\text{max}}$  is still significant. Finally, it is interesting to note that, for both the thin and thick discs, the migrator and non-migrator subsamples (dotted and dashed lines) have similar  $z_{\text{max}}$  distributions as the total samples (solid thick).

#### 4 N-BODY+SPH SIMULATION OF A CLUMPY GALAXY

We now explore an  $N$ -body+Smooth Particle Hydrodynamics (SPH) simulation of the formation of an isolated galaxy which forms clumps in its early evolution. In these clumps, the star formation rate density is high and supernovae type II rapidly enrich the surrounding medium with  $\alpha$ -elements. The clumps scatter  $\alpha$ -rich stars to high  $|z|$  ( $\alpha$ -poor stars are also scattered, but they are born further the clumps and therefore are less likely to be strongly scattered), giving rise to a geometric thick disc (similar to the mechanism proposed by Bournaud et al. 2009). After  $\approx 4$  Gyr, the clumps stop forming because of the declining gas mass fraction and any remaining clumps are either disrupted or sink to the centre; thus clumps only affect the early evolution of the galaxy. This scenario was recently shown to naturally produce a chemical bimodality (Clarke et al. 2019), density profiles (Beraldo e Silva et al. 2020) and a Splash population (Amarante et al. 2020b) very similar to those observed in the

MW (Holtzman et al. 2018; Mackereth et al. 2017; Belokurov et al. 2020). Finally, as mentioned in the Introduction, this scenario naturally predicts a co-formation of the thin and thick discs.

In this section, we first show that the clump scenario reproduces the observational trends discussed above. Then, we analyze the simulation’s time evolution to unravel the secular evolution driving the Milky Way to exhibit those trends.

##### 4.1 Simulation details

For the initial conditions, we use a  $5\times$  higher mass resolution version of that described in Clarke et al. (2019). A gas corona with  $5 \times 10^6$  particles in hydrostatic equilibrium is placed within an NFW (Navarro et al. 1997) dark matter halo which constitutes 90% of the total mass. The virial radius and mass of the dark matter halo are  $r_{200} \approx 200$  kpc and  $M_{200} = 10^{12} M_{\odot}$ , respectively, and it also has  $5 \times 10^6$  particles. While the gas corona has the same radial density profile, it constitutes only 10% of the mass. No additional baryons or stars are present at  $t = 0$ . The spin parameter of the gas corona is set to  $\lambda = 0.065$  (Bullock et al. 2001). The gas corona and the dark matter halo have softening lengths of  $\epsilon = 50$  pc and  $\epsilon = 100$  pc, respectively. Star particles forming from the gas also have a softening of  $\epsilon = 50$  pc.

These initial conditions are evolved for 13 Gyr with GASOLINE (Wadsley et al. 2004, 2017) with sub-grid models for the gas cooling, star formation and feedback. Gas cooling includes the metal-line cooling of Shen et al. (2010). The gas cools and settles into a disc. Once its density exceeds a certain threshold (set to  $0.1 \text{ cm}^{-3}$ ), star formation

starts (with an efficiency set to 5%) from gas particles with temperature below 15,000 K which are part of a converging flow. We use the blast wave supernova feedback (Stinson et al. 2006), which couples, as thermal energy, 10% of the  $10^{51}$  erg per supernova to the interstellar medium. Gas mixing uses turbulent diffusion as described by Shen et al. (2010). A base timestep of  $\Delta t = 5$  Myr is used, with timesteps refined such that  $\delta t = \Delta t/2^n < \eta\sqrt{\epsilon/a_g}$ , where we set the refinement parameter  $\eta = 0.175$ . We set the opening angle (for the tree-code gravity calculation) to  $\theta = 0.7$ . The timesteps of gas particles additionally satisfy the condition  $\delta t_{\text{gas}} = \eta_{\text{courant}} h / [(1+\alpha)c + \beta\mu_{\text{max}}]$ , where  $\eta_{\text{courant}} = 0.4$ ,  $h$  is the SPH smoothing length set over the 32 nearest neighbour particles,  $\alpha$  and  $\beta$  are the linear and quadratic viscosity coefficients and  $\mu_{\text{max}}$  is described by Wadsley et al. (2004).

Oxygen and iron yields from SNII and SNIa are taken from Raiteri et al. (1996). As in Raiteri et al. (1996), we use Padova stellar lifetimes to determine SNII rates, while SNIa rates are determined from those same lifetimes in a binary evolution model.

We use data from the last snapshot, at 13 Gyr, and select star particles older than 10 Gyr at the Solar torus, i.e. within a torus defined by circles at  $R = 8 \pm 2$  kpc, for an approximate match with the selection criteria used for the MW. For brevity, we will refer to this region as the Solar Neighbourhood in the simulation. We compute the total gravitational potential at this final snapshot and integrate each orbit for 10 dynamical times using AGAMA (Vasiliev 2019). Finally, we calculate pericenter and apocenter radii, as well as eccentricities, using Eq. (1), and  $z_{\text{max}}$ .

## 4.2 Simulation results and comparison to the MW

Fig. 4 shows a 2D histogram in the abundance map ( $[\text{O}/\text{Fe}]$  vs  $[\text{Fe}/\text{H}]$ ) for old star particles ( $\tau > 10$  Gyr) produced in the simulation. The immediate conclusion from this plot is that, as in the MW, the simulated galaxy has already developed the chemical bi-modality associated to the thick/thin discs in the very first Gyrs of its evolution, indicating a rapid formation of the thick and thin discs. The straight lines in this plot are traced to define chemical thick and thin discs (above and below the dashed lines, respectively) to be used in the subsequent analysis, similar to those defined in the MW – see Fig. 2 (upper panel). The thick disc comprises 37% and the thin disc, 49% of the total. If we instead select star particles older than 11 Gyr, we have 49% for thick disc and 34% for thin disc. Although these numbers do not match in detail the fractions obtained in the cross-match with APOGEE-DR16 (see Fig. 2 and Table A1), they can be considered as a good approximation, given the uncertainties and possible selection effects in the observational data and the intrinsic simplicity of a simulated isolated galaxy.

Fig. 5 (upper panel) shows the distribution of stars in the  $r_{\text{per}}$  vs  $e$  plane of the simulation ( $N = 531,519$  star particles). As in the MW (Fig. 1), the data peak along a line of approximately constant  $r_{\text{apo}}$ , at  $8 \lesssim r_{\text{apo}}/\text{kpc} \lesssim 9$ , and is mostly concentrated in the region  $6 \lesssim r_{\text{apo}}/\text{kpc} \lesssim 14$  (dashed lines), reflecting the same selection effects present in our MW sample, as described in Sec. 3.1. The bottom panel shows the  $r_{\text{per}}$  KDE for this sample (full grey) and after the restriction to the region  $6 \lesssim r_{\text{apo}}/\text{kpc} \lesssim 14$  (dashed black), which reduces the sample to  $N = 513,907$  star particles. We

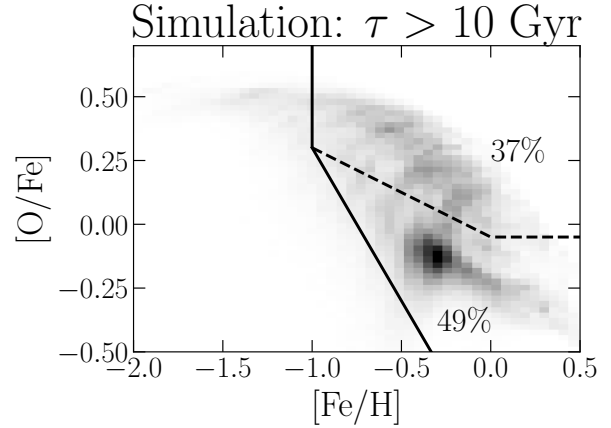


**Figure 4.** 2D histogram in chemical space for old stars in the simulation. Like in the MW (Fig. 2), a chemical bi-modality is already present in the very first Gyrs of evolution. Dashed lines define the chemical thick and thin discs.

can see that this restriction leaves the KDE essentially identical to the original one. We use this restriction in the rest of the analysis for the same reason as we did with the MW data, i.e. to avoid orbits with extreme or unrealistic kinematic properties, which can be introduced by the assumed potential.

Note that the simulated galaxy lacks the first peak at  $r_{\text{per}} \approx 0.5$  kpc, which in the MW is associated with the accreted halo; this identification is strengthened by the fact that the simulated galaxy evolves in isolation, with no accretion events. The two other peaks observed in the MW are clearly present in the simulation, at  $r_{\text{per}} \approx 3.5$  kpc and  $r_{\text{per}} \approx 6$  kpc, respectively. The positions of these peaks differ from those in the MW (see Fig. 1), as well as the eccentricity values at the peaks. However, these differences are not fundamentally important for our conclusions, since we are interested in comparing the trends, while the simulated galaxy is not intended to be an exact replica of the MW. Next, we show that indeed these two peaks are mostly, but not only, composed of thick and thin disc stars, respectively. For a better comparison with the MW, in what follows we exclude the most metal-poor star-particles, i.e. those to the left of the solid line in Fig. 4.

Fig. 6 shows the KDE of the kinematic quantities and chemical abundances obtained in the simulation, for the thick disc (upper panels) and thin disc (bottom panels), to be compared to Fig. 3. The left-hand column shows that the  $r_{\text{per}}$  distributions of both thin and thick discs are bimodal: the thick disc peaks at  $r_{\text{per}} \approx 3$  kpc and has a bump at  $r_{\text{per}} \approx 6$  kpc, while the thin disc has a peak at  $r_{\text{per}} \approx 4$  kpc and another, of slightly larger amplitude, at  $r_{\text{per}} \approx 6$  kpc. The relative amplitudes of these peaks and bumps show a good agreement with those observed in the MW – see Fig. 3.

We repeat the procedure used for the MW and use a GMM to split the  $r_{\text{per}}$  distributions of the thin and thick discs into two Gaussian components each (dashed and dotted curves in the left panels). Then, for subsamples defined according to the highest probability of belonging to one or the other Gaussian component, we calculate the KDEs of other quantities, shown in the respective panels of Fig. 6.

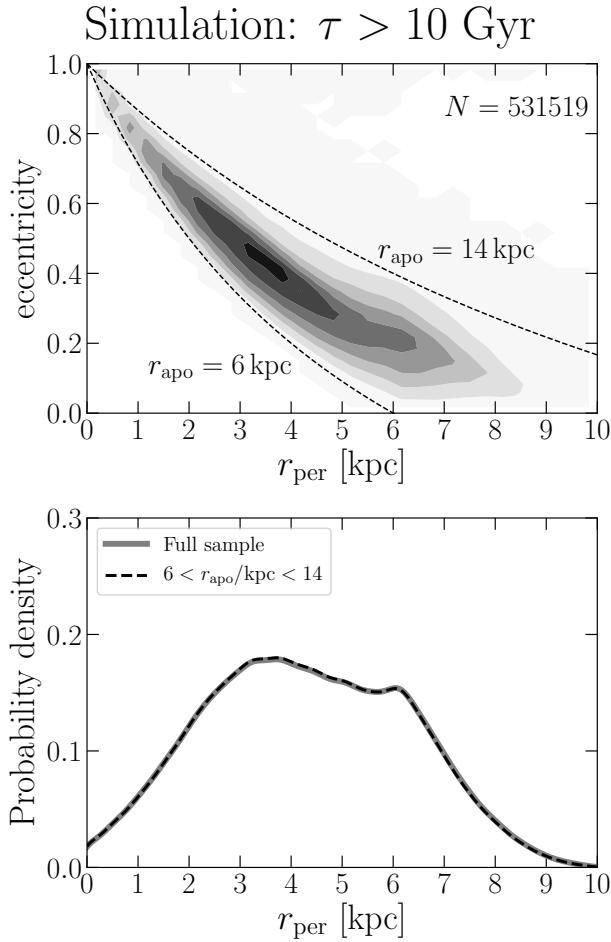


**Figure 5.** Top: distribution of old stars in eccentricity,  $e$ , vs pericentric radius,  $r_{\text{per}}$ , for the Solar Neighbourhood of the simulation. Bottom: KDEs of  $r_{\text{per}}$ : for the full sample (grey) and for  $6 < r_{\text{per}}/\text{kpc} < 14$  (black dashed). As in the MW (Fig. 1), we identify two peaks, mainly (but not only) associated with, from left to right, the thick and thin disc, respectively. The peak associated to the accreted halo in the MW is not present, since the simulated galaxy evolves in isolation.

The second column shows that the eccentricities in the thin disc peak at  $e \approx 0.2$  and have a narrower distribution than the thick disc, which peaks at  $e \approx 0.35$ . However, the thin disc has a tail for large eccentricities and both distributions are broader than those in the MW (second column in Fig. 3).

The third and fourth columns show the KDEs for  $[\text{Fe}/\text{H}]$  and  $[\text{O}/\text{Fe}]$ , respectively. The subsamples (dotted and dashed lines) have KDEs very similar to the total samples, indicating that, as in the MW, the peaks and bumps in the  $r_{\text{per}}$  distribution are not due to contamination between the thin and thick discs. Finally, the right-hand column shows the  $z_{\text{max}}$  distribution. The thick disc distribution is broader than that of the thin disc. It is interesting to note that the simulation  $z_{\text{max}}$  KDE is bi-modal, while this bi-modality is apparently not present in Fig. 3. However, this bi-modality, associated to discrete tracks in a plot of  $z_{\text{max}}$  vs  $r_{\text{apo}}$ , has been observed in larger samples in the MW (Haywood et al.

2018), and shown to result from the presence of different orbital families in the adopted axisymmetric potential model – see Amarante et al. (2020a).

Thus, we conclude that the simulation is able to reproduce the features observed for the old stars in the MW, mainly:

- in the very first Gyrs of evolution, the galaxy already has a well established chemical bi-modality comprised of the thin and thick discs, with relative contributions comparable to those in the MW;
- the  $r_{\text{per}}$  distribution has two peaks that can be mainly attributed to the thin and thick discs, although both peaks have contributions from both discs and this is not due to contamination;
- $\sim 1/2$  of the thin disc stars are associated to the high  $r_{\text{per}}$  peak (at  $\approx 7$  kpc in the MW and at  $\approx 6$  kpc in the simulation), while that fraction is  $\sim 1/3$  for the thick disc;
- stars that mostly contribute to the high  $r_{\text{per}}$  peak are those with smaller eccentricities; and finally,
- a significant fraction of chemical thick disc stars have low  $z_{\text{max}}$ , i.e. overlap with the geometric thin disc.

In what follows, we analyze the evolution of the simulation to show that stars contributing to the high  $r_{\text{per}}$  peak formed at smaller radii and moved outwards due to radial migration, suggesting that the same happened in the MW.

### 4.3 Time evolution and radial migration

#### 4.3.1 Migrators all over the disc

We start this section by comparing the current position (at  $t = 13$  Gyr) of old star particles on nearly-circular orbits with the position they had at  $t = 5$  Gyr. This earliest snapshot is chosen right after the early turbulent period when the clumps are still present, since we are now interested in the subsequent secular evolution. We select star particles older than 10 Gyr, but without any geometric cut. For each particle we calculate the so-called circularity  $\lambda_c = L_z/L_c(E)$ , where  $L_z$  is the  $z$ -component of angular momentum and  $L_c(E)$  is the angular momentum of a circular orbit at the same energy  $E$ . Then, we select particles on nearly-circular orbits ( $\lambda_c > 0.9$ ) and split this sample into chemical thin and thick discs (as defined in Fig. 4).

Fig. 7 shows 2D histograms of the cylindrical radius at different times,  $R(t = 13 \text{ Gyr})$  vs  $R(t = 5 \text{ Gyr})$  for this sample, split into thin (left) and thick (right) discs. Colours in the top row represent total numbers, while the histograms in the bottom row are column-normalized. If particles kept on orbits at the same radii they had at early times, they would concentrate along the diagonal dashed line. However, we observe a large spread, i.e. large changes in radii, with a significant fraction of particles changing radii by several kpc. Since we select particles on nearly-circular orbits, we suppress from these plots the possibility of migration by blurring, i.e. by oscillations around the guiding radii. Thus, Fig. 7 shows the effect of radial migration (churning) all over the disc, i.e. particles moving from nearly-circular orbits to other nearly-circular orbits, as originally proposed by Sellwood & Binney (2002). Importantly, although the number of nearly-circular orbits in the thick disc is smaller than in the thin disc, as shown in the top panels, those orbits are

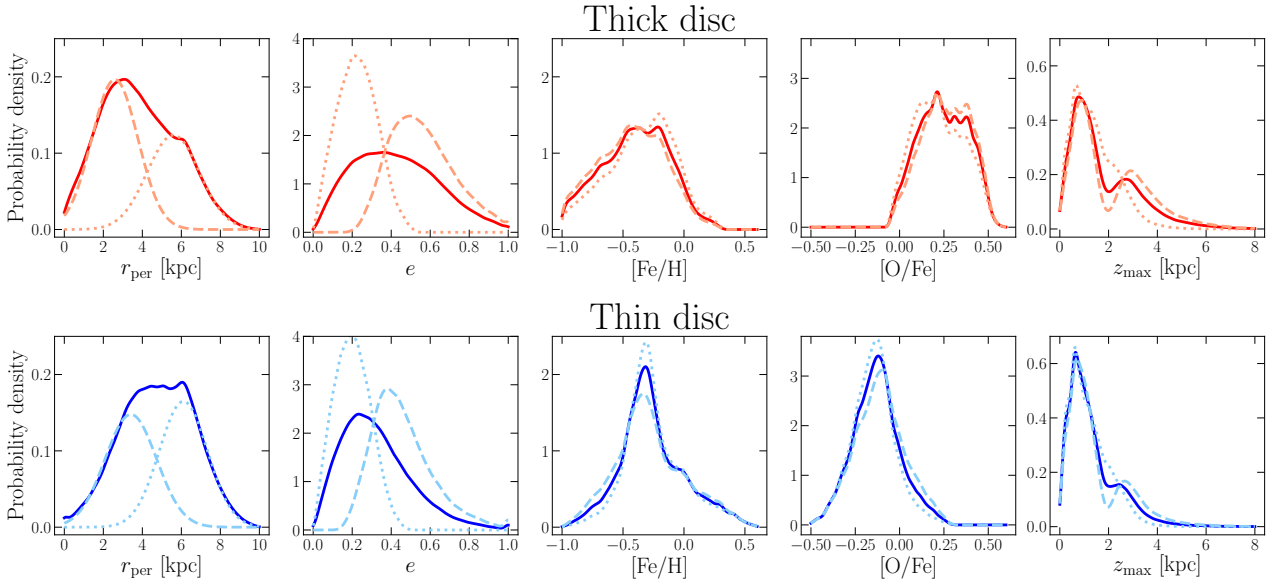


**Figure 6.** KDEs for kinematic quantities and chemical abundances for the chemical thin and thick discs in the simulation. As in the MW (Fig. 3), both discs have two peaks/bumps in the  $r_{\text{per}}$  distribution, split into the two Gaussians shown as dotted and dashed curves in the first column. In the other columns, dotted and dashed curves show the KDEs of the respective quantities for these two subsamples. The larger  $r_{\text{per}}$  subsample (dotted lines) is characterized by lower eccentricities while the lower  $r_{\text{per}}$  subsample (dashed lines) is characterized by higher eccentricities. As in the MW, the chemical abundance distributions of these subsamples are very similar to that of the total sample for each disc, suggesting that the  $r_{\text{per}}$  peaks/bumps are not due to contamination from the thin/thick discs. The relative amplitudes of the two  $r_{\text{per}}$  peaks/bumps in the thin and thick discs are similar those observed in the MW – see Fig. 3.

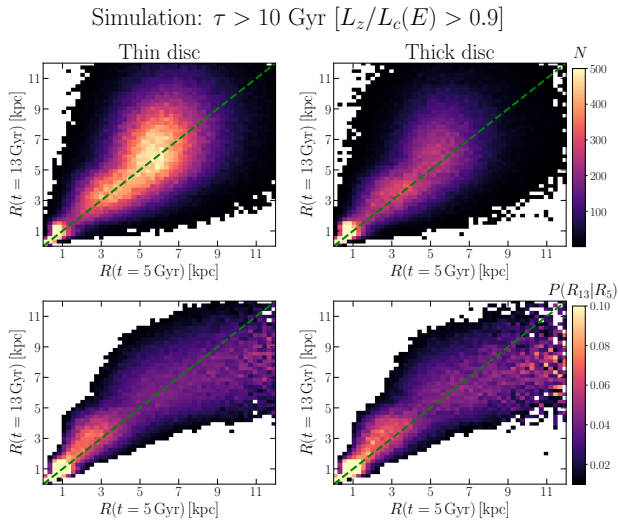


**Figure 7.** 2D histograms of (cylindrical) radii  $R(t = 13 \text{ Gyr})$  vs  $R(t = 5 \text{ Gyr})$  for old star particles on nearly-circular orbits, split into thin/thick discs (left/right). The top panels are colour-coded by total numbers, while the bottom panels are column-normalized. The large spread around the diagonal shows the effect of radial migration (churning) produced by spiral arms. Radial migration affects the thin and thick discs similarly, although particles on nearly-circular orbits (those most affected) are less numerous in the thick disc.

similarly affected by radial migration in the two discs, as shown in the bottom panels.

For a more compact representation of the effect of radial migration, we calculate the change  $\Delta R \equiv R(13 \text{ Gyr}) - R(5 \text{ Gyr})$  for each star particle on nearly-circular orbits (as previously defined) and estimate the KDE of  $\Delta R$ , which is shown in Fig. 8, with the blue (red) curve representing the thin (thick) disc. It is clear that the two discs are similarly affected by radial migration: both KDEs have a narrow peak near  $\Delta R = 0$ , and are positively skewed, i.e. have a longer tail to the right, indicating a net movement outwards, a consequence of the density decrease outwards. The root-mean-square (rms) change in radius is  $\sim 2.3 \text{ kpc}$  for the thin disc (similar to the value found by Roškar et al. 2008) and  $\sim 2.1 \text{ kpc}$  for the thick disc. This can be contrasted with the rms radial change due to radial migration modelled by Frankel et al. (2020). With a sample spanning  $5 \lesssim R/\text{kpc} \lesssim 13$ , these authors find that for MW thin disc stars  $\langle (\Delta R)^2 \rangle^{1/2} \sim 2.6 \text{ kpc} \sqrt{\tau/6 \text{ Gyr}}$ . For  $\tau = 8 \text{ Gyr}$  (the time between the two simulation snapshots we are considering), this results in  $\langle (\Delta R)^2 \rangle^{1/2} \sim 3 \text{ kpc}$ , while applying the same geometric cut in the simulation, we find  $\langle (\Delta R)^2 \rangle^{1/2} \sim 2.6 \text{ kpc}$  for the thin disc. We conclude that the extent of migration in the simulation is comparable to that of the MW.

#### 4.3.2 Migrators in the Solar Neighbourhood

Having shown the effect of radial migration all over the thin and thick discs, we now investigate its role in producing the high  $r_{\text{per}}$  peak shown in Figs. 1, 3, 5 and 6. We go back to the original geometric cut and select, in the final snapshot

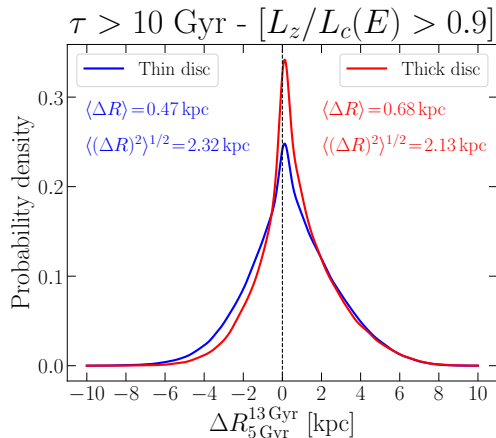


**Figure 8.** KDEs of  $\Delta R \equiv R(t = 13 \text{ Gyr}) - R(t = 5 \text{ Gyr})$  for the thin (blue) and thick (red) discs. Both KDEs peak near  $\Delta R = 0$ , but have long tails, with star particles migrating by several kpc. The positive skewness indicate a net movement outwards.

( $t = 13 \text{ Gyr}$ ), star particles older than 10 Gyr in the Solar Neighbourhood (a torus defined by circles at  $R = 8 \pm 2 \text{ kpc}$ ). Then, we track these same particles at different snapshots from 5 Gyr to 13 Gyr. At each snapshot, we integrate the particles orbits in the respective potentials and determine the peri and apo-center radii and eccentricity for each particle. Finally, we calculate the KDE of these quantities at each snapshot.

Fig. 9 (two left columns) shows the  $r_{\text{per}}$  KDEs (solid lines) for the thin disc (blue) and thick disc (red) at different snapshots (rows). Similarly to the procedure used in Figs. 3 and 6, at the final snapshot (bottom panels), we split our  $r_{\text{per}}$  sample into two Gaussian components using a GMM (dashed and dotted curves in the bottom panels) and use these components to define two subsamples. Then, for these fixed subsamples we calculate, at each snapshot, the  $r_{\text{per}}$  KDEs, shown as dotted and dashed curves in the remaining plots (weighted according to the Gaussian weights obtained at the final snapshot).

At 5 Gyr, for both the thin and thick discs, the full sample distributions (thick solid lines) are unimodal, peaking at  $r_{\text{per}} \approx 4 \text{ kpc}$  for the thin disc and at  $r_{\text{per}} \approx 3 \text{ kpc}$  for the thick disc, which must reflect differences in average formation radii for these two components. From top to bottom panels, we see that while the positions of these peaks are approximately conserved, the distributions get progressively positively skewed, until another peak appears at  $r_{\text{per}} \approx 6 \text{ kpc}$  for the thin disc and a bump at this same location for the thick disc.

For both the thin and thick discs, while the low  $r_{\text{per}}$  Gaussian component (dashed) stays approximately fixed at the same position for different snapshots, the high  $r_{\text{per}}$  component (dotted) moves to the right and becomes skewed to large values, producing the high  $r_{\text{per}}$  peak at the final snapshot. This shows that the high  $r_{\text{per}}$  peak is characterized by stars which, on average, formed in inner radii and move outwards. The hashed regions in Fig. 9 are defined as those star-particles which, at the final time, have  $r_{\text{per}} > 7 \text{ kpc}$  ( $r_{\text{per}} > 6 \text{ kpc}$ ) for the thin (thick) disc. These are the values

beyond which the contribution from the low  $r_{\text{per}}$  peak Gaussian component is negligible, thus showing the effect of migration in a cleaner way, with some star-particles moving at least 4 kpc outwards in 2 Gyrs (from 11 Gyr to 13 Gyr).

Besides the general tendency of a net movement outwards observed in Sec. 4.3.1, this is a consequence of the inside-out growth of the galactic disc and the fact that we are selecting old stars in the Solar Neighbourhood, which was poorly populated at early stages of the galaxy. Stars can visit the Solar Neighbourhood by oscillating around their guiding radius (blurring, most relevant for eccentric orbits) or via radial migration (churning). As already mentioned in Sec. 3.3, the two most important features of radial migration is that it is more effective for low-eccentricity orbits and that it does not significantly change these eccentricities. In other words, radial migration (churning) typically moves stars from circular orbits to other circular orbits (Sellwood & Binney 2002; Roškar et al. 2012). In Fig. 6, we showed that the high  $r_{\text{per}}$  component is the one with the lower eccentricities, in agreement with the MW (Fig. 3). Moreover, Fig. 9 (two right columns) shows the KDEs of the eccentricity at the same times and for the same samples as in the left panels. The eccentricities for those stars which will produce the high  $r_{\text{per}}$  peak in the left panels (dotted lines) do not show a significant evolution. On the other hand, it is interesting to note that the other subsample, which will produce the low  $r_{\text{per}}$  peak in the two left columns (dashed lines) shows some evolution over time, moving the left-hand tail to the right, i.e. with any low-eccentricity orbits gradually becoming more eccentric (heating).

Therefore, these results strongly suggest that the process responsible for moving that population outwards and producing the high  $r_{\text{per}}$  peak (in both the simulation and in the MW) is radial migration (churning), which justifies calling this population ‘the migrators’ (and calling the low  $r_{\text{per}}$  peak ‘the non-migrators’).

## 5 DISCUSSION

### 5.1 Implications for the disc formation

As mentioned in the Introduction, some theoretical models predict a sequential formation of thin and thick discs, with the thin disc becoming a significant component only after the thick disc has formed. In such scenarios, one should not expect to find a significant population of old thin disc stars. In Sec. 3 we showed several lines of evidence for such a population in the MW – see Figs. 2 and 3, with thin (thick) disc stars comprising 29% (54%) of the sample. The existence of a significant old thin disc population suggests that the thin disc starts forming earlier than generally assumed, having a large formation time overlap with the thick disc, and this is the main result of this work. Therefore, models which predict a sequential formation of the thin/thick discs, such as the upside-down scenario, are disfavored by our results. Also disfavoring this scenario is our finding of a large fraction of chemical thick disc stars with low  $z_{\text{max}}$  (peaking at  $z_{\text{max}} \approx 1 \text{ kpc}$  – see Fig. A1), which suggests two possible explanations: either, in line with the upside-down scenario, these low  $z_{\text{max}}$  stars were born at high  $|z|$  and settled to the geometric thin disc, or the chemical thick disc stars were

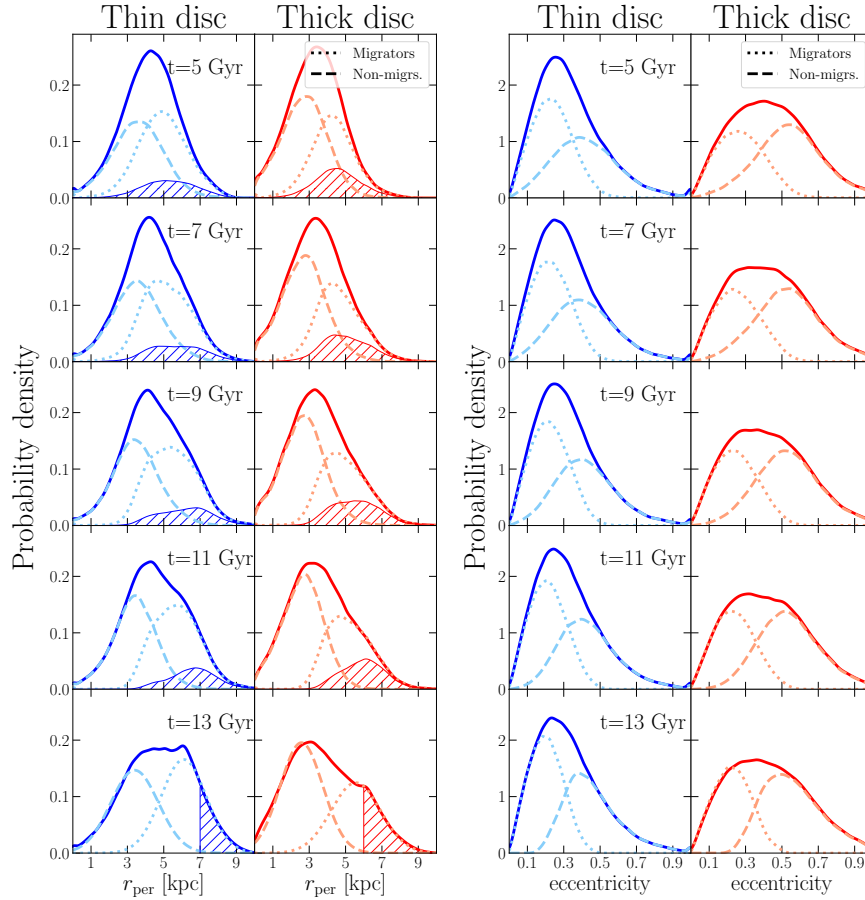


**Figure 9.** Left: time evolution of the  $r_{\text{per}}$  KDE in the thin (blue) and thick (red) discs of the simulation. Old star-particles ( $\tau > 10$  Gyr) are selected and split into two Gaussians at  $t = 13$  Gyr, and these fixed samples and subsamples are analyzed at earlier times (the same particles are considered in all snapshots). Right: time evolution of the eccentricities KDE in the thin and thick discs for the same fixed samples defined in the left panels. In both thin and thick discs, the low  $r_{\text{per}}$  subsample (dashed lines) is that associated to higher eccentricities (as shown in the right panels), and thus is less affected by radial migration, staying approximately fixed in place (the non-migrators). The high  $r_{\text{per}}$  subsample (dotted lines) is that on nearly-circular orbits, and thus is significantly affected by radial migration and tends to move outwards (the migrators) and to develop a positive skewness. At  $t = 13$  Gyr, the migrators produce the high  $r_{\text{per}}$  peaks. The hatched areas show samples selected at  $t = 13$  Gyr as those with  $r_{\text{per}} > 7$  kpc ( $r_{\text{per}} > 6$  kpc) for the thin (thick) disc, just to show the effect in a cleaner sample, i.e. less contaminated by non-migrators. Overall, the migrators eccentricity distributions (dotted lines) are conserved over the evolution. This agrees with expectations for radial migration, which changes orbits guiding radii without kinematically heating them. On the other hand, the non-migrators exhibit some heating, with nearly-circular orbits at  $t = 5$  Gyr getting more eccentric with time.

born at low  $|z|$  and a fraction of these stars were scattered to high  $|z|$ , leaving a significant fraction at low  $z_{\text{max}}$ . Since stars constitute a collisionless component, one expects them to get kinematically hotter under secular evolution (unless some fine-tuned mechanism is advocated to kinematically cool these stars), thus making the second possibility more plausible.

On the other hand, some models do predict an early co-formation of thin and thick discs and thus the existence of a conspicuous old thin disc population. For instance, in the accretion model, Abadi et al. (2003) predict that 15% of the current thin disc stars should be older than 10 Gyr. In this picture the old thin disc population is built up from several disrupted satellites, each with unique chemical signatures, merger geometry and kinematics. Thus, Abadi et al. (2003) predicted that this old thin disc population should show dis-

tinct chemo-kinematic substructures or correlations. In our sample of old stars, the subsamples of stars classified as migrators and non-migrators (based on  $r_{\text{per}}$ , which is similar to splitting by eccentricity) have chemical abundance distributions very similar to the total samples – see Fig. 3. This suggests that the correlations predicted in the accretion scenario are not observed in the MW.

In the major merger scenario (Quinn et al. 1993; Villalobos & Helmi 2008; Helmi et al. 2018), the thick disc is produced by one major merger whose progenitor is massive enough to vertically heat a proto-disc, and consequently an old thin disc remnant is expected. Villalobos & Helmi (2008) predict that the mass fraction of this remnant thin disc is 15% – 25% of the total stellar mass at the end of the merger. Note that this prediction refers to a geometric definition of the thin disc, while the chemically defined thin disc is gen-

erally seen as forming only after the merger (see e.g. [Grand et al. 2020](#)), in which case the significant old chemical thin disc population found in this work is unexpected. On the other hand, if a chemical thin disc population were present in the proto-disc, a significant fraction of these stars should have been vertically heated and should have large  $z_{\max}$ , similar to thick disc stars. However, the thin disc  $z_{\max}$  distribution does not extend as much as the thick disc to large values (compare the dashed curves in Fig. A1, where we select stars with  $|z| < 6$  kpc). Thus, also the major merger scenario seems disfavored by our results. Additionally, possible concerns with this scenario have been recently raised on the basis of asteroseismic age estimates of thick disc stars. [Montalbán et al. \(2020\)](#) applied this technique to estimate ages (within  $\sim 10\%$ ) of a sample of metal poor stars ( $[\text{Fe}/\text{H}] < -0.5$ ), finding that part (if not all) of thick disc stars are as old as (or even slightly older than) the stars accreted in the last major merger, thus concluding that this event was not the main trigger to the formation of the thick disc.

Whatever the case may be, these discussions suggest that the formation of the thick disc is still puzzling and this should motivate further studies of alternative scenarios. A compelling possibility is offered by the clumpy scenario explored in our simulation (Sec. 4). In this scenario, the early galaxy forms clumps and there are two main star formation channels:  $\alpha$ -rich stars are born in clumps and tend to be scattered to high  $|z|$  and reasonably large eccentricities (forming the thick disc), while the formation of  $\alpha$ -poor stars is more broadly distributed over the disc. This scenario has been shown to generate a chemical bi-modality, geometric thin+thick discs and a Splash population in good agreement with those observed in the MW ([Clarke et al. 2019](#); [Beraldo e Silva et al. 2020](#); [Amarante et al. 2020b](#)). Most importantly, a direct prediction of this scenario is an early start for the thin disc formation, with a large time overlap with the thick disc formation – see Fig. 11 from [Clarke et al. \(2019\)](#). Additionally, this scenario also naturally predicts that a fraction of the chemical thick disc should overlap with the geometric thin disc, i.e. should have low  $z_{\max}$ , as we found in this work for the MW – see Fig. A1.

## 5.2 Radial migration: thin disc vs thick disc

The analysis of Sec. 4.3 showed evidence for the role of radial migration in the simulation, changing the guiding radii of stars in nearly-circular orbits typically by  $\langle(\Delta R)^2\rangle^{1/2} \sim 2$  kpc in a few Gyr. We showed that a consequence of this is the appearance of a peak in the  $r_{\text{per}}$  distribution of old stars, with properties very similar to those found in the MW. Interestingly, this evidence is present in *both* the thin and thick discs – see Fig. 9.

Going back to Fig. 6, we can now evaluate differences in the relevance of radial migration for the thin and thick discs. As already mentioned, the migrators are characterized by low eccentricities, while non-migrators are characterized by higher eccentricities. On the other hand, inside the thin or thick discs, the  $z_{\max}$  distribution in our simulation (right-hand panels in Fig. 6) is similar for migrators and non-migrators (dashed and dotted curves). This shows that whether a star will be affected by radial migration depends essentially on its eccentricity, but not much on its vertical excursion amplitude, in agreement with the conclusions of

[Solway et al. \(2012\)](#). In other words, the extent to which thin and thick discs are differently affected by radial migration is determined by their eccentricity distributions, and not by their different scale heights: the thin disc is more affected by radial migration because most of its orbits have low eccentricities, while the fraction of nearly-circular orbits in the thick disc is lower and it is in this sense that one can say that the thick disc is less affected by radial migration. In fact, for particles in nearly-circular orbits all over the disc, thin and thick discs are equally affected by radial migration – see Fig. 8. Moreover, selecting particles at the Solar Neighbourhood, and judging by the similarity of the  $r_{\text{per}}$  KDEs of thin and thick discs at 5 Gyr (Fig. 9) and the similar positions of the high  $r_{\text{per}}$  peak (due to migrators) at 13 Gyr, one can say that the *migrators* in both the thin and thick discs are equally influenced by radial migration, i.e. move by similar amounts in the same time interval.

In a recent paper, [Mikkola et al. \(2020\)](#) also concluded that the vertical excursions are not of much relevance to radial migration in simulated galaxies if the disc is more dominant with respect to the dark matter halo, while vertical excursions can be more relevant to radial migration for galaxies with more dominant halos. Thus, the relative contribution of the disc and halo masses can have some importance on our results regarding the simulated galaxy and the MW. Interestingly, [Cole & Binney \(2017\)](#) find that baryons dominate the MW’s gravitational potential in the disc out to about the Solar Neighbourhood, which, considering the conclusions of [Mikkola et al. \(2020\)](#), reinforces our finding of a significant migration in the thick disc of the MW.

## 5.3 The conundrum of RR Lyrae in the thin disc

As discussed in the Introduction, in sequential formation scenarios, where the thin disc only forms after the thick disc has formed, RR Lyrae (which have ages  $\gtrsim 10$  Gyr) are not expected to be found in the thin disc. The recent detection of a population of thin disc RR Lyrae then appears as a conundrum ([Prudil et al. 2020](#)) in such scenarios. One solution of this conundrum was proposed by [Iorio & Belokurov \(2020\)](#). Using a sample of  $\sim 70,000$  RR Lyrae in *Gaia*-DR2, they confirmed a sub-population with high rotational velocity and low  $|z|$ , typical of the thin disc. They found that their velocity dispersion is almost a factor of 2 smaller than that of a sample with age  $\tau = 10$  Gyr; comparing with the empirically determined age-velocity dispersion relation of [Sharma et al. \(2020\)](#), they concluded that this population has velocity dispersion similar to that of a 2 Gyr-old population. They suggested that these might be some other population of stars which mimics RR Lyrae. We note, however, that a rotationally selected sample is by definition kinematically biased (towards small velocity dispersions), while the sample used by [Sharma et al. \(2020\)](#) to fit the AVR is complete, and this could potentially lead to the conclusion of a younger population.

The solution of this conundrum provided by our results is that a thin disc population of old RR Lyrae is not a problem in the first place. Our results show that the existence of these old thin disc stars suggests an early co-formation of thin and thick discs, a scenario in which the existence of RR Lyrae in the thin disc is naturally accommodated. In this sense the RR Lyrae are no different from other old pop-

ulations of stars, a fraction of which is also  $\alpha$ -poor, thin and rapidly rotating like the thin disc.

## 6 CONCLUSIONS

In this work, we use the catalogue of Sanders & Das (2018) and select old stars ( $\tau > 10$  Gyr) within 2 kpc from the Sun. After applying several quality cuts, our final sample consists of  $N = 23,795$  (turnoffs + giants) stars with full 6-D phase-space coordinates from *Gaia*-DR2. We use these to integrate orbits in an assumed Galactic potential, determining peri and apo-center radii, eccentricities and maximum vertical excursions. For a smaller sub-sample of  $N = 1049$  (turnoffs + giants) stars, we obtain [Mg/Fe] and [Fe/H] abundances from APOGEE-DR16 and chemically split this subsample into halo, thin and thick disc stars. At the end, we compare the obtained results with those from a simulated galaxy which forms clumps in its early evolution. Our main conclusions are summarized below:

- Chemical thin disc stars represent a significant fraction of our sample of old stars, with star counts comparable to those of the chemical thick disc – see Table A1. We interpret this as evidence that the thin disc formation starts early, with a large time overlap with the formation of the thick disc.
- The  $r_{\text{per}}$  distribution of old stars has three peaks, one at  $r_{\text{per}} \approx 0.59$  kpc, one at  $r_{\text{per}} \approx 5.4$  kpc and another at  $r_{\text{per}} \approx 7.14$  kpc. This confirms the findings of Prudil et al. (2020), who showed evidence for three  $r_{\text{per}}$  peaks using a sample with 314 RR Lyrae stars.
- The first peak (at  $r_{\text{per}} \approx 0.59$  kpc) is associated to the stellar halo. The other two peaks have distinct contributions from both the thin and thick discs;
- In both the thin and thick discs, stars contributing to the second  $r_{\text{per}}$  peak are those with higher eccentricities, while stars contributing to the third  $r_{\text{per}}$  peak are those on nearly-circular orbits. We suggest (and confirm with the simulation) that the third peak is produced by stars which migrated from inner radii, while the second peak is mostly due to non-migrating stars.
- In the Solar Neighbourhood,  $\sim 1/2$  of the old thin disc stars can be classified as migrators, while for the thick disc this fraction is reduced to  $\sim 1/3$ .
- Thin and thick discs are differently affected by radial migration inasmuch as they have different eccentricity distributions. Therefore, thick disc stars on nearly-circular orbits are as affected by radial migration as thin disc stars in nearly-circular orbits.
- Our results disfavor sequential formation models, such as the upside-down scenario, where the thin disc only starts to be significant after the thick disc is formed.
- Among the models which predict an early co-formation of thin and thick discs, the clumpy star formation scenario seems to be favoured by our results, which is demonstrated by a good agreement between observational and simulated trends.

## ACKNOWLEDGEMENTS

We thank Eugene Vasiliev for help in the use of the AGAMA library. We also thank Giuliano Iorio and Vasily Belokurov by discussions on their analysis of RR-Lyrae stars. VPD and LBS are supported by STFC Consolidated grant # ST/R000786/1. The simulations in this paper were run at the DiRAC Shared Memory Processing system at the University of Cambridge, operated by the COSMOS Project at the Department of Applied Mathematics and Theoretical Physics on behalf of the STFC DiRAC HPC Facility ([www.dirac.ac.uk](http://www.dirac.ac.uk)). This equipment was funded by BIS National E-infrastructure capital grant ST/J005673/1, STFC capital grant ST/H008586/1 and STFC DiRAC Operations grant ST/K00333X/1. DiRAC is part of the National E-Infrastructure. J.A. acknowledges The World Academy of Sciences and the Chinese Academy of Sciences for the CAS-TWAS fellowship.

## DATA AVAILABILITY

The Sanders & Das dataset is publicly available from [this URL](#). APOGEE-DR16 stellar abundances are available at [this URL](#). The simulation dataset used here is proprietary but can be shared for limited use on request to V.P.D. ([vpde-battista@gmail.com](mailto:vpde-battista@gmail.com)).

## REFERENCES

- Abadi M. G., Navarro J. F., Steinmetz M., Eke V. R., 2003, *ApJ*, **597**, 21
- Adibekyan V. Z., Santos N. C., Sousa S. G., Israelian G., 2011, *AAP*, **535**, L11
- Agertz O., et al., 2020, arXiv e-prints, [p. arXiv:2006.06008](#)
- Ahumada R., Allende Prieto C., Almeida A., et al., 2020, *ApJS*, **249**, 3
- Amarante J. A. S., Smith M. C., Boeche C., 2020a, *MNRAS*, **492**, 3816
- Amarante J. A. S., Beraldo e Silva L., Debattista V. P., Smith M. C., 2020b, *ApJL*, **891**, L30
- Anders F., et al., 2014, *AAP*, **564**, A115
- Belokurov V., Erkal D., Evans N. W., Koposov S. E., Deason A. J., 2018, *MNRAS*, **478**, 611
- Belokurov V., Sanders J. L., Fattahi A., et al., 2020, *MNRAS*, **494**, 3880
- Bensby T., Feltzing S., Oey M. S., 2014, *AAP*, **562**, A71
- Beraldo e Silva L., Debattista V. P., Khachatryan T., Nidever D., 2020, *MNRAS*, **492**, 4716
- Bird J. C., Kazantzidis S., Weinberg D. H., Guedes J., Callegari S., Mayer L., Madau P., 2013, *ApJ*, **773**, 43
- Bournaud F., Elmegreen B. G., Martig M., 2009, *ApJL*, **707**, L1
- Bovy J., Rix H.-W., Liu C., Hogg D. W., Beers T. C., Lee Y. S., 2012, *ApJ*, **753**, 148
- Bovy J., Rix H.-W., Schlafly E. F., Nidever D. L., Holtzman J. A., Shetrone M., Beers T. C., 2016, *ApJ*, **823**, 30
- Brook C. B., Kawata D., Gibson B. K., Freeman K. C., 2004, *ApJ*, **612**, 894
- Bullock J. S., Dekel A., Kolatt T. S., Kravtsov A. V., Klypin A. A., Porciani C., Primack J. R., 2001, *ApJ*, **555**, 240
- Chiappini C., Matteucci F., Romano D., 2001, *ApJ*, **554**, 1044
- Ciucă I., Kawata D., Miglio A., Davies G. R., Grand R. J. J., 2020, arXiv e-prints, [p. arXiv:2003.03316](#)
- Clarke A. J., et al., 2019, *MNRAS*, **484**, 3476
- Cole D. R., Binney J., 2017, *MNRAS*, **465**, 798

Frankel N., Sanders J., Ting Y.-S., Rix H.-W., 2020, *ApJ*, **896**, 15

Gilmore G., Reid N., 1983, *MNRAS*, **202**, 1025

Glatt K., et al., 2008, *AJ*, **135**, 1106

Grand R. J. J., et al., 2020, arXiv e-prints, p. [arXiv:2001.06009](https://arxiv.org/abs/2001.06009)

Hall P., York M., 2001, *Statistica Sinica*, **11**, 515

Hayden M. R., et al., 2015, *ApJ*, **808**, 132

Haywood M., Di Matteo P., Lehnert M. D., Snaith O., Khoperskov S., Gómez A., 2018, *ApJ*, **863**, 113

Helmi A., Babusiaux C., Koppelman H. H., Massari D., Veljanoski J., Brown A. G. A., 2018, *Nature*, **563**, 85

Holtzman J. A., et al., 2018, *AJ*, **156**, 125

Iorio G., Belokurov V., 2020, arXiv e-prints, p. [arXiv:2008.02280](https://arxiv.org/abs/2008.02280)

Ivezić Ž., Connelly A. J., VanderPlas J. T., Gray A., 2014, *Statistics, Data Mining, and Machine Learning in Astronomy*

Jönsson H., et al., 2020, arXiv e-prints, p. [arXiv:2007.05537](https://arxiv.org/abs/2007.05537)

Kazantzidis S., Bullock J. S., Zentner A. R., Kravtsov A. V., Moustakas L. A., 2008, *ApJ*, **688**, 254

Loebman S. R., Roškar R., Debattista V. P., Ivezić Ž., Quinn T. R., Wadsley J., 2011, *ApJ*, **737**, 8

Loebman S. R., Debattista V. P., Nidever D. L., Hayden M. R., Holtzman J. A., Clarke A. J., Roškar R., Valluri M., 2016, *ApJL*, **818**, L6

Mackereth J. T., et al., 2017, *MNRAS*, **471**, 3057

Mackereth J. T., et al., 2019, *MNRAS*, **482**, 3426

McMillan P. J., 2017, *MNRAS*, **465**, 76

Meng X., Gnedin O. Y., 2020, arXiv e-prints, p. [arXiv:2006.10642](https://arxiv.org/abs/2006.10642)

Mikkola D., McMillan P. J., Hobbs D., 2020, *MNRAS*, **495**, 3295

Montalbán J., et al., 2020, arXiv e-prints, p. [arXiv:2006.01783](https://arxiv.org/abs/2006.01783)

Muñoz-Mateos J. C., Gil de Paz A., Boissier S., Zamorano J., Jarrett T., Gallego J., Madore B. F., 2007, *apJ*, **658**, 1006

Navarro J. F., Frenk C. S., White S. D. M., 1997, *ApJ*, **490**, 493

Nidever D. L., et al., 2014, *ApJ*, **796**, 38

Pedregosa F., et al., 2011, *Journal of Machine Learning Research*, **12**, 2825

Prudil Z., Dékány I., Grebel E. K., Kunder A., 2020, *MNRAS*, **492**, 3408

Quinn P. J., Hernquist L., Fullagar D. P., 1993, *ApJ*, **403**, 74

Raiteri C. M., Villata M., Navarro J. F., 1996, *AAP*, **315**, 105

Rojas-Arriagada A., Zoccali M., Schultheis M., Recio-Blanco A., Zasowski G., Minniti D., Jönsson H., Cohen R. E., 2019, *AAP*, **626**, A16

Roškar R., Debattista V. P., Stinson G. S., Quinn T. R., Kaufmann T., Wadsley J., 2008, *ApJL*, **675**, L65

Roškar R., Debattista V. P., Quinn T. R., Wadsley J., 2012, *MNRAS*, **426**, 2089

Sanders J. L., Das P., 2018, *MNRAS*, **481**, 4093

Schönrich R., Binney J., 2009a, *MNRAS*, **396**, 203

Schönrich R., Binney J., 2009b, *MNRAS*, **399**, 1145

Sellwood J. A., Binney J. J., 2002, *MNRAS*, **336**, 785

Sharma S., et al., 2020, arXiv e-prints, p. [arXiv:2004.06556](https://arxiv.org/abs/2004.06556)

Shen S., Wadsley J., Stinson G., 2010, *MNRAS*, **407**, 1581

Silverman B. W., 1981, *J. Roy. Stat. Soc.*, **43**, 97

Solway M., Sellwood J. A., Schönrich R., 2012, *MNRAS*, **422**, 1363

Stinson G., Seth A., Katz N., Wadsley J., Governato F., Quinn T., 2006, *MNRAS*, **373**, 1074

VandenBerg D. A., Brogaard K., Leaman R., Casagrande L., 2013, *ApJ*, **775**, 134

Vasiliev E., 2019, *MNRAS*, **482**, 1525

Vickers J. J., Smith M. C., 2018, *ApJ*, **860**, 91

Villalobos Á., Helmi A., 2008, *MNRAS*, **391**, 1806

Wadsley J. W., Stadel J., Quinn T., 2004, *NA*, **9**, 137

Wadsley J. W., Keller B. W., Quinn T. R., 2017, *MNRAS*, **471**, 2357

Yoshii Y., 1982, *PASJ*, **34**, 365

$\tau$ [Gyr]	$d$ [kpc]	$ R-R_{\odot} $ [kpc]	$ z $ [kpc]	$N$	Thick	Thin
$> 10$	$< 0.5$	—	—	222	40%	50%
	<b><math>&lt; 2</math></b>	—	—	<b>1049</b>	<b>54%</b>	<b>29%</b>
	—	$< 2$	$< 2$	1489	52%	26%
			$< 6$	2238	46%	17%
			<b><math>0.3 &lt;  z  &lt; 6</math></b> <b><math>&lt; 0.3</math></b>	<b>1909</b> <b>330</b>	<b>48%</b> <b>37%</b>	<b>12%</b> <b>54%</b>
$> 11$	$< 0.5$	—	—	124	46%	37%
	<b><math>&lt; 2</math></b>	—	—	<b>573</b>	<b>54%</b>	<b>25%</b>
	—	$< 2$	$< 2$	759	48%	25%
			$< 6$	1036	41%	18%
			<b><math>0.3 &lt;  z  &lt; 6</math></b> <b><math>&lt; 0.3</math></b>	<b>849</b> <b>187</b>	<b>41%</b> <b>38%</b>	<b>12%</b> <b>48%</b>

**Table A1.** Simple estimates of the effect of selection effects in the cross-match with APOGEE-DR14: for different age and geometric cuts, the right-hand columns show the fractions of thin and thick disc stars compared to the total sample (including halo stars, not shown). The fiducial cut for  $\tau > 10$  Gyr, and the corresponding one with  $\tau > 11$  Gyr, are shown in boldface. Cuts intended to suppress (inflate) the thin disc contribution are shown in red (blue). The fraction of thin disc stars is  $\gtrsim 17\%$ , even considering cuts intended to suppress the thin disc.

## APPENDIX A: GEOMETRIC CUTS AND SELECTION EFFECTS

In Sec. 3.2, we present the fractions for the thin and thick discs in our sample of old stars in the fiducial cut (ages  $\tau > 10$  Gyr and distances  $d < 2$  kpc). This cut obviously introduces some selection effects and that fractions should not be seen at face values. In this appendix, we make a simple evaluation of the selection effects by varying the cuts and recalculating those fractions. Additionally to the fiducial cut, we select stars with  $\tau > 11$  Gyr and within the Solar cylinder, i.e. ( $|R-R_{\odot}| < 2$  kpc) and different cuts in  $|z|$ . The number counts in the cross-match with APOGEE and the fractions of thin and thick disc stars for different combinations of these cuts are shown in Table A1. Generally speaking, the thin disc stars correspond to  $\sim 20 - 30\%$  of the samples (with slightly larger or smaller fractions for cuts intended to suppress or increase the thin disc contribution), while the thick disc corresponds to  $\sim 40 - 55\%$ . Regardless of exact values, this indicates that the thin disc represents a significant component of the old Milky Way.

Another finding of this paper is the significant fraction of chemical thick disc stars in the region of the geometric thin disc, i.e. at small  $z_{\max}$ . This could in principle be flawed by the suppression of thick disc stars with large  $z_{\max}$  in the fiducial cut. Fig. A1 shows that the thick disc indeed extends to high  $z_{\max}$  when selecting stars with  $|z| < 6$  kpc (dashed red curve). However, its distribution still peaks at  $z_{\max} \sim 1$  kpc and has a significant population with low  $z_{\max}$ .

This paper has been typeset from a  $\text{\LaTeX}$  file prepared by the author.

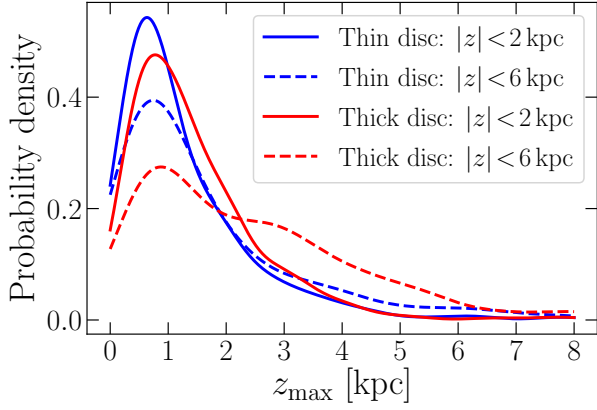


**Figure A1.** KDE of  $z_{\max}$  for old stars in the thin and thick discs (blue and red, respectively) in the cross-match with APOGEE-DR14 within cylindrical regions around the Sun ( $R - R_{\odot} < 2$  kpc) – see Table A1 for details. While the thin disc KDE is changed for the different cuts, the thick disc extends to much larger  $z_{\max}$  when we select stars with  $|z| < 6$  kpc. However, even in this case, a significant fraction of chemical thick disc stars are confined to the geometric thin disc, i.e. have low  $z_{\max}$ .